Turbulence measurements in the bubbly flow region of hydraulic jumps

Serhat Kucukali [a],[*], Hubert Chanson [b]

[a] Division of Civil Engineering, Zonguldak Karaelmas University, Zonguldak, Turkey
[b] Division of Civil Engineering, The University of Queensland, Brisbane QLD 4072, Australia

ARTICLE INFO

ABSTRACT

A hydraulic jump is characterized by a highly turbulent flow with macro-scale vortices, some kinetic energy dissipation and a bubbly two-phase flow structure. New air–water flow measurements were performed in a large-size facility using two types of phase-detection intrusive probes: i.e. single-tip and double-tip conductivity probes. These were complemented by some measurements of free-surface fluctuations using ultrasonic displacement meters. The void fraction measurements showed the presence of an advective diffusion shear layer in which the void fractions profiles matched closely an analytical solution of the advective diffusion equation for air bubbles. The free-surface fluctuations measurements showed large turbulent fluctuations that reflected the dynamic, unsteady structure of the hydraulic jumps. The measurements of interfacial velocity and turbulence level distributions provided new information on the turbulent velocity field in the highly-aerated shear region. The velocity profiles tended to follow a wall jet flow pattern. The air–water turbulent integral time and length scales were deduced from some auto- and cross-correlation analyses based upon the method of Chanson [H. Chanson, Bubbly flow structure in hydraulic jump, Eur. J. Mech. B/Fluids 26 (3) (2007) 367–384], providing the turbulent scales of the eddy structures advecting the air bubbles in the developing shear layer. The length scale L_{xz} is an integral air–water turbulence length scale which characterized the transverse size of the large vortical structures advecting the air bubbles. The experimental data showed that the dimensionless integral turbulent length scale L_{xz}/d_1 was closely related to the inflow depth: i.e. $L_{xz}/d_1 = 0.2–0.8$, with L_{xz} increasing towards the free-surface.

1. Introduction

A hydraulic jump is the rapid transformation of a supercritical open channel flow into a fluvial regime. It is characterized by a highly turbulent flow with macro-scale vortices, some significant kinetic energy dissipation and a bubbly two-phase flow region (Fig. 1). Fig. 1A shows a definition sketch of the hydraulic jump flow while Fig. 1B presents a photograph of hydraulic jump. The hydraulic jump is typically characterized by its inflow Froude number Fr_1 defined as

$$Fr_1 = \frac{U_1}{\sqrt{g \times d_1}} \qquad (1)$$

where U_1 is the depth-averaged upstream flow velocity, d_1 is the upstream flow depth, and g is the gravity acceleration. In a hydraulic jump, the inflow Froude number is always greater than unity [1–3]. In a hydraulic jump, the flow singularity at the impingement point induces some air entrainment (Fig. 1). The air bubble entrainment has some important implication in terms of interactions with the turbulence structure and air–water mass transfer, including

oxygen transfer. Void fractions measurements in hydraulic jumps were first conducted by Rajaratnam [4]. Resch and Leutheusser [5] showed the effect of the inflow conditions on the void fraction profiles. More recent studies included Mossa and Tolve [6], Chanson and Brattberg [7], Murzyn et al. [8] and Chanson [9] (Table 1). Turbulence characteristics in hydraulic jumps were investigated by Rouse et al. [10], Resch and Leutheusser [5], Chanson and Brattberg [7], Liu et al. [11] and Chanson [9,12]. These studies suggested that the turbulence levels were large in the developing shear layer, and that maximum values were observed shortly downstream of the jump toe. In recent studies, Mouaze et al. [13], Chanson [9] and Murzyn and Chanson [14] identified some turbulent length scales in hydraulic jumps.

The aim of the present study is to examine thoroughly the air–water turbulent flow properties in hydraulic jumps with relatively large inflow Froude numbers $4.7 \leqslant Fr_1 \leqslant 8.5$. Both the free-surface fluctuations and turbulent length and time scales were investigated altogether.

2. Experimental facility and instrumentation

New experiments were carried out in a 0.50 m wide, 0.45 m deep horizontal rectangular flume, with 3.2 m long glass sidewalls

* Corresponding author.
E-mail address: serhatkucukali@karaelmas.edu.tr (S. Kucukali).

Nomenclature

C	air concentration defined as the volume of air per unit volume of air
D_t	turbulent diffusivity (m²/s) of air bubbles in air–water flow
D'_t	turbulent diffusivity (m²/s) of air bubbles in interfacial free-surface aerated flow
$D^\#$	dimensionless turbulent diffusivity: $D^\# = D_t/(U_1 * d_1)$
D	(1) flow depth (m) measured perpendicular to the flow direction (2) clear-water flow depth defined as: $d = \int_{C=0\%}^{C=90\%}(1-C) \times dy$
d_c	critical flow depth
d_{mean}	mean flow depth
d_{std}	standard deviation of the flow depth
$(d_{std})_{max}$	maximum standard deviation of the flow depth along the hydraulic jump
d_1	flow depth (m) measured immediately upstream of the hydraulic jump
d_2	flow depth (m) measured immediately downstream of the hydraulic jump
F	air bubble count rate (Hz) or bubble frequency defined as the number of detected air bubbles per unit time
F_{max}	maximum bubble count rate (Hz) at a given cross-section
Fr_1	upstream Froude number: $Fr_1 = \frac{U_1}{\sqrt{g \times d_1}}$
g	gravity constant: $g = 9.80$ m/s² in Brisbane, Australia
L_j	hydraulic jump length (m)
L_{xz}	transverse air–water length scale (m): $L_{xx} = \int_{z=0}^{z=z((R_{xz})_{max}=0)}(R_{xz})_{max} \times d\tau$
N_{ab}	number of air bubbles per record
Q	water discharge (m³/s)
q_w	water discharge per unit width (m²/s)
Re	Reynolds number: $Re = \frac{U_1 \times d_1}{v}$
R_{xx}	normalized auto-correlation function (reference probe)
R_{xz}	normalized cross-correlation function between two probe output signals
$(R_{xz})_{max}$	maximum cross-correlation between two probe output signals
Tu	turbulence intensity defined as: $Tu = u'/V$
T	average air–water interfacial travel time between the two probe sensors
T_{Int}	characteristic integral time scale: $T_{Int} = \int_{z=0}^{z=z((R_{xz})_{max}=0)}(R_{xz})_{max} \times T_{xz} \times dz$
T_{xx}	auto-correlation integral time scale: $T_{xx} = \int_{\tau=0}^{v=\tau(R_{xx}=0)} R_{xx} \times d\tau$
T_{xz}	cross-correlation integral time scale: $T_{xz} = \int_{\tau=\tau(R_{xz}=(R_{xz})_{max})}^{v=\tau(R_{xz}=0)} R_{xz} \times d\tau$
$(T_{0.5})_{xx}$	characteristic time lag τ for which $R_{xx} = 0.5$
$(T_{0.5})_{xz}$	characteristic time lag τ for which $R_{xz} = 0.5 * (R_{xz})_{max}$
u'	root mean square of longitudinal component of turbulent velocity (m/s)
V	local velocity (m/s)
V_{max}	maximum velocity (m/s) at outer edge of boundary layer
U_1	depth-averaged flow velocities upstream the hydraulic jump (m/s): $U_1 = q_w/d_1$
W	channel width (m)
x	longitudinal distance from the sluice gate (m)
x_1	longitudinal distance from the gate to the jump toe (m)
$Y_{C_{max}}$	distance (m) normal to the jet support where $C = C_{max}$
$Y_{F_{max}}$	distance (m) normal to the jet support where $F = F_{max}$
y	distance (m) measured normal to the channel bed
z	transverse distance (m) from the channel centerline
z_{max}	transverse distance (m) where the cross-correlation coefficient tends to zero
δ	boundary layer thickness (m) defined in term of 99% of the maximum velocity: $\delta = y(V = 0.99 * V_{max})$
Δx	longitudinal distance between probe sensors
v	kinematic viscosity of water (m²/s)
ρ	density (kg/m³)
σ	surface tension between air and water (N/m)
τ	time lag (s)

and a PVC bed (Fig. 1B). The channel was previously used by Chanson [9,12].

The water discharge was measured with a Venturi meter located in the supply line and it was calibrated on-site with a large V-notch weir. The discharge measurement was accurate within ±2%. The clear-water flow depths were measured using rail mounted point gauges with a 0.2 mm accuracy. The free-surface fluctuations were recorded using five ultrasonic displacement meters Microsonic™ Mic+25/IU/TC with an accuracy of 0.18 mm and a response time of 50 ms, and an ultrasonic displacement meter Microsonic™ Mic+35/IU/TC with an accuracy of 0.18 mm and a response time of 70 ms. The displacement meters were mounted above the flow and scanned downward the air–water flow "pseudo" free-surface. The Mic+35 sensor sampled the free-surface of the supercritical inflow, while the Mic+25 sensors were located above the jump roller. Each probe signal output was scanned at 50 Hz per sensor for 20 min. The positions of the six acoustic displacement meters are: $(x - x_1)/d_1 = -8.33$; 4.17; 8.75; 13.33; 17.92 and 33.

The air–water flow properties were measured with either two single type conductivity probes ($\varnothing = 0.35$ mm) or a double-tip conductivity probe ($\varnothing = 0.25$ mm, $\Delta x = 7.0$ mm). The probes were manufactured at the University of Queensland. The conductivity probe is a phase-detection intrusive probe designed to pierce the bubbles. The phase-detection relies on the difference in electrical resistance between air and water [15,16]. Herein the probes were excited by an electronic system (Ref. UQ82.518) designed with a response time of less than 10 μs. During the experiments, each probe sensor was sampled at 10 kHz for 48 s. When two single-tip conductivity probes were used simultaneously, the reference probe was located on the channel centerline ($z = 0$) while the second identical probe was separated in the transverse direction by a known spacing z using the method of Chanson [9,12] (Fig. 2). Both probe sensors were located at the same vertical and streamwise distances y and x, respectively. The probe displacement in the vertical direction was controlled by a fine adjustment system connected to a Mitutoyo™ digimatic scale unit with a vertical accuracy Δy of less than 0.1 mm.

2.1. Data processing

2.1.1. Free-surface fluctuations measurements

The ultrasonic displacement probes were calibrated with clear-water at rest against pointer gauge measurements for a range of water depths shortly before each experiment. Koch and Chanson [17] used the same sensors and applied this calibration technique. They compared successfully the acoustic displacement readings with instantaneous free-surface profiles captured with a high-speed camera. Note that each sensor was set with no filter and for multiplex mode.

With any ultrasonic displacement meter, the signal output is a function of the strength of the acoustic signal reflected by the
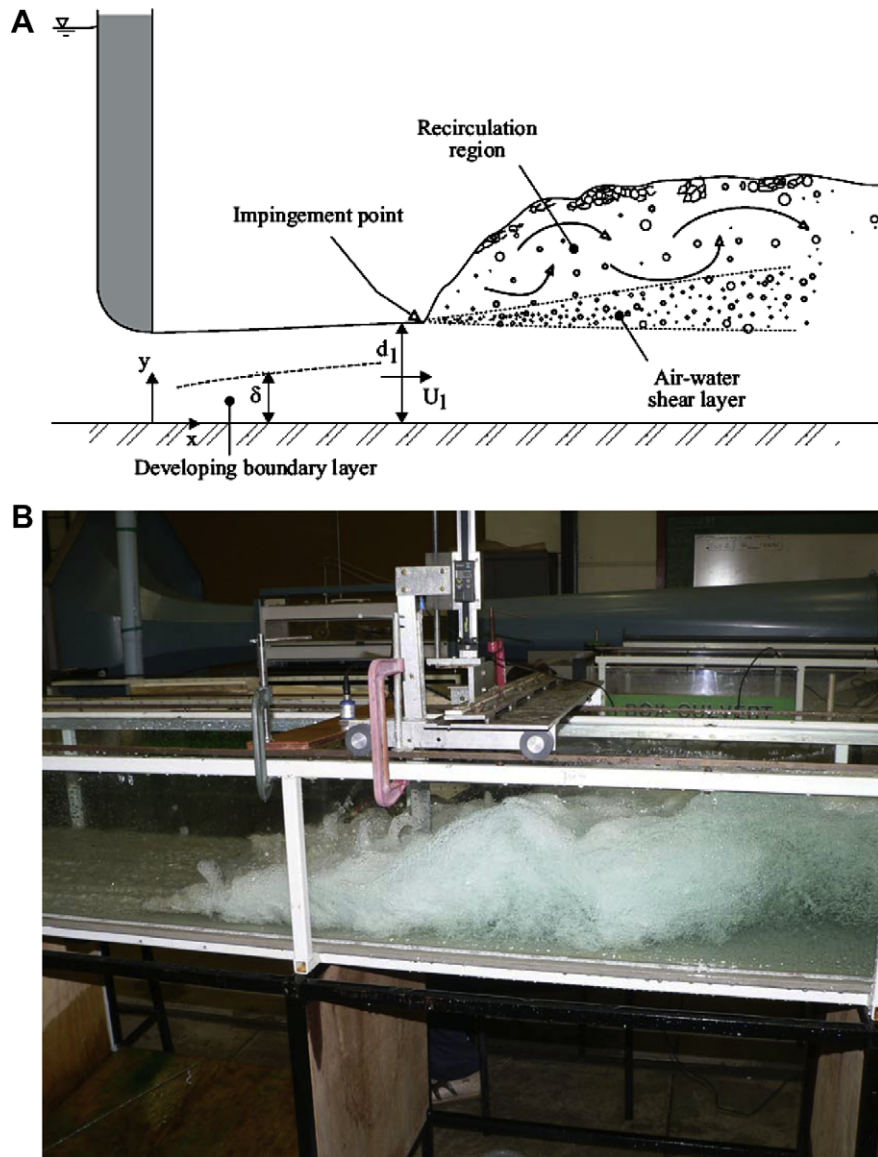
Fig. 1. Hydraulic jump with partially-developed inflow conditions: (A) definition sketch; (B) photograph of a hydraulic jump: $Fr_1 = 7$, $x_1 = 1$ m, $W = 0.5$ m, shutter speed: 1/80 s, flow from left to right, with a single-tip conductivity probe and an acoustic displacement meter sampling at $x = 1.2$ m.

"free-surface". Some erroneous points may be recorded when the free-surface is not horizontal and in bubbly flows. Chanson et al. [18] tested an ultrasonic displacement meter Keyence™ UD300 in a bubbly column with up to 10% void fraction. Their results suggested that the ultrasonic probe readings corresponded to about Y_{50} to Y_{60}, where Y_{xx} is the elevation where the void fraction is $xx\%$. During the present study, a comparison between ultrasonic probe outputs and conductivity probe data showed that the ultrasonic probe reading gave a depth corresponding to about Y_{60} to Y_{80} in the hydraulic jump roller. When measurements were made in the roller or downstream of the toe for largest Froude numbers. In this case, some data errors were caused by bubbles, water splashes and droplets coming into contact with the sensitive part of the acoustic displacement meter. Herein, the data were filtered to remove and replace erroneous points.

2.1.2. Conductivity probes

The air–water flow properties were calculated using a single threshold technique and the threshold was set at about 45–55% of the air–water voltage range (error <1% on void fraction). The ba-

sic probe outputs were the void fraction, or air concentration C, the bubble count rate F defined as the number of bubbles impacting the probe-tip per second, and the air chord time distribution where the chord time is defined as the time spent by the bubble on the probe-tip [19]. The statistical analyses of chord time distributions yielded the mean chord time, median, standard deviation, skewness and kurtosis. When two probe sensors were simultaneously sampled, the signals were analysed in terms of the auto-correlation and cross-correlation functions R_{xx} and R_{xz}, respectively (Fig. 2). With the double-tip probe, the cross-correlation calculation gives the air–water interfacial velocity V [16,20]. The time-averaged velocity equals

$$V = \frac{\Delta x}{T} \tag{2}$$

where Δx is the longitudinal distance between probe sensors and T is the average air–water interfacial travel time between the two probe sensors. The turbulence levels were derived from the relative width of the cross-correlation function compared to that of the auto-correlation function

Table 1
Recent experimental investigations of air entrainment in hydraulic jumps with partially-developed inflow conditions

Reference (1)	x_1 m (2)	d_1 m (3)	Fr_1 (4)	Re (5)	Instrumentation (6)	W m (7)
[7]	0.50	0.014	6.3 and 8.5	3.3×10^4 and 4.4×10^4	Pitot tube (3.3 mm Ø), conductivity probe (double-tip, 0.025 mm inner electrode)	0.25
[8]	–	0.021–0.059	2.0–4.8	1.6×10^4 to 8.8×10^4	Optical fibre probe (double-tip, 0.010 mm Ø)	0.3
[9,12]	0.50	0.013	5.1–8.5	2.5×10^4 and 7.7×10^4	Conductivity probes (single-tip, 0.35 mm inner electrode)	0.25
	1.0	0.025–0.029	5.1–8.6	3.8×10^4 to 9.8×10^4		0.25
	1.0	0.024–0.026	5.1 and 8.5	6.8×10^4 to 9.8×10^4		0.50
Present study	1.0	0.024	4.7–8.5	5×10^4 to 9.8×10^4	Conductivity probes (single-tip, 0.35 mm inner electrode; double-tip conductivity probe, 0.25 mm inner electrode), ultrasonic displacement meters	0.5

Notes: F/D: fully-developed; P/D: partially-developed; and (–): information not available.

$$Tu = 0.851 \times \frac{\sqrt{\tau_{0.5}^2 - T_{0.5}^2}}{T} \tag{3}$$

where $\tau_{0.5}$ is the time scale for which the normalized cross-correlation function is half of its maximum value such as: $R_{xz}(T + \tau_{0.5}) = 0.5 \times (R_{xz})_{max}$, $(R_{xz})_{max}$ is the maximum cross-correlation function for $\tau = T$, and $T_{0.5}$ is the characteristic time for which the normalized auto-correlation function equals: $R_{xx}(T_{0.5}) = 0.5$ [21]. The turbulence level Tu characterizes the fluctuations of the air–water interfacial velocity between the probe sensors. When two single-tip probes, separated by a known transverse distance z, were simultaneously sampled, the correlation analysis results included the maximum cross-correlation coefficient $(R_{xz})_{max}$, and the integral time scales T_{xx} and T_{xz} defined as

$$T_{xx} = \int_{\tau=0}^{v=\tau(R_{xx}=0)} R_{xx} \times d\tau \tag{4}$$

$$T_{xz} = \int_{\tau=\tau(R_{xz}=(R_{xz})_{max})}^{v=\tau(R_{xz}=0)} R_{xz} \times d\tau \tag{5}$$

where τ is the time lag, R_{xx} is the normalized auto-correlation function of the reference probe signal, and R_{xz} is the normalized cross-correlation function between the two probe signals. T_{xx} represented an integral time scale of the longitudinal bubbly flow structures (Fig. 2). It was a characteristic time of the large eddies advecting the air–water interfaces in the longitudinal direction. T_{xz} was a characteristic time scale of the vortices with a transverse length scale z [9].

In the present study, identical experiments were repeated with different separation distances z, and a characteristic integral length scale L_{xz}, and the associated integral time scale T_{Int}, were calculated as

$$L_{xz} = \int_{z=0}^{z=z((R_{xz})_{max}=0)} (R_{xz})_{max} \times dz \tag{6}$$

$$T_{Int} = \int_{z=0}^{z=z((R_{xz})_{max}=0)} (R_{xz})_{max} \times T_{xz} \times dz \tag{7}$$

The length scale L_{xz} represented an integral turbulent length scale of the large vortical structures advecting the air bubbles in the hydraulic jump flow [9,22]. The turbulent time scale T_{Int} was the associated integral turbulent time scale but Eq. (7) is not a dimensionally homogenous equation.
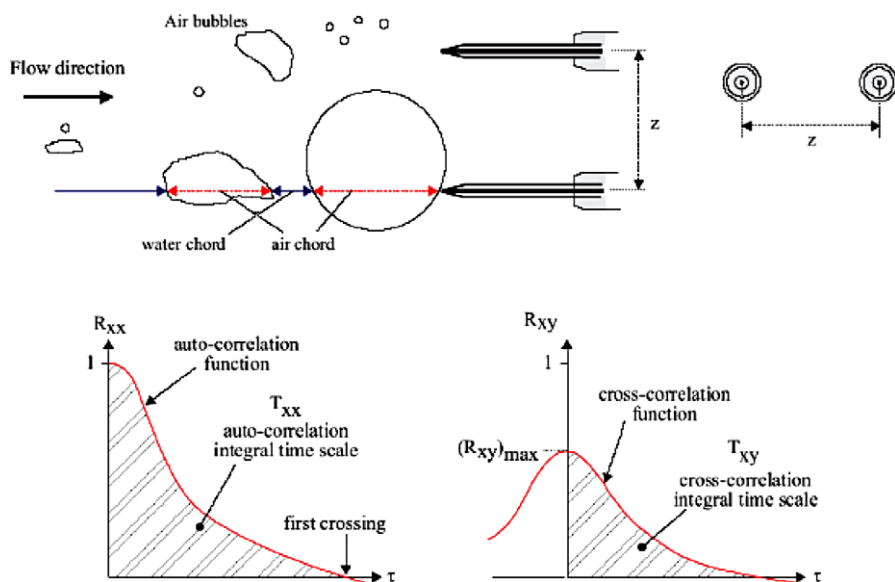

Fig. 2. Sketch of two-phase-detection probes separated by a transverse distance.

Table 2
Experimental flow conditions

x_1 (m)	d_1 (m)	Q (m³/s)	d_2	L_j (m)	U_1 (m/s)	Re	Fr_1	Remarks
1.0	0.024	0.0273	0.150	0.50	2.28	5×10^4	4.7	Free-surface and air–water flow measurements
1.0	0.024	0.0291	0.165	0.52	2.42	6×10^4	5.0	Free-surface measurements
1.0	0.024	0.0337	0.192	0.62	2.81	7×10^4	5.8	Free-surface and air–water flow measurements
1.0	0.024	0.0402	0.230	0.80	3.35	8×10^4	6.9	Free-surface and air–water flow measurements incl. velocity measurements
1.0	0.024	0.0495	0.262	1.0	4.12	1×10^5	8.5	Free-surface measurements

2.2. Experimental flow conditions

Several hydraulic jump flows were tested (Table 2). The jump toe location was controlled by an upstream rounded gate and by a downstream overshoot gate (Fig. 1). All the experiments were carried out with the same inflow depth ($d_1 = 0.024$ m) and the same distance from the upstream gate ($x_1 = 1$ m). The inflow was characterized by a partially-developed boundary layer ($\delta/d_1 \sim 0.4$–0.6). Details of the experiments are listed in Table 2, where Q is the water discharge, d_2 is the downstream conjugate depth, L_j is the measured jump length and Re is the inflow Reynolds number defined as

$$Re = \frac{U_1 \times d_1}{v} \tag{8}$$

with v the kinematic viscosity of water.

The free-surface measurements were conducted for $Fr_1 = 4.7$–8.5 (Table 2). The air–water flow measurements were performed for: $Fr_1 = 4.7$, 5.8 and 6.9. The velocity and turbulence measurements were performed for $Fr_1 = 6.9$. The air–water flow properties were measured in the developing air–water flow region (i.e. $(x - x_1)/d_1 < 25$) where the upstream depth d_1 was measured typically 0.10–0.20 m upstream of the jump toe. Full details of the data sets were reported in [22].

3. Flow patterns and free-surface fluctuations

The hydraulic jump was a sharp flow discontinuity associated with strong turbulent structures, intense air bubble entrainment, and some significant spray and splashing. This was clearly observed in the large-size facility and it is seen in the photograph (Fig. 1B). At the impingement point, air packets were entrained in a developing
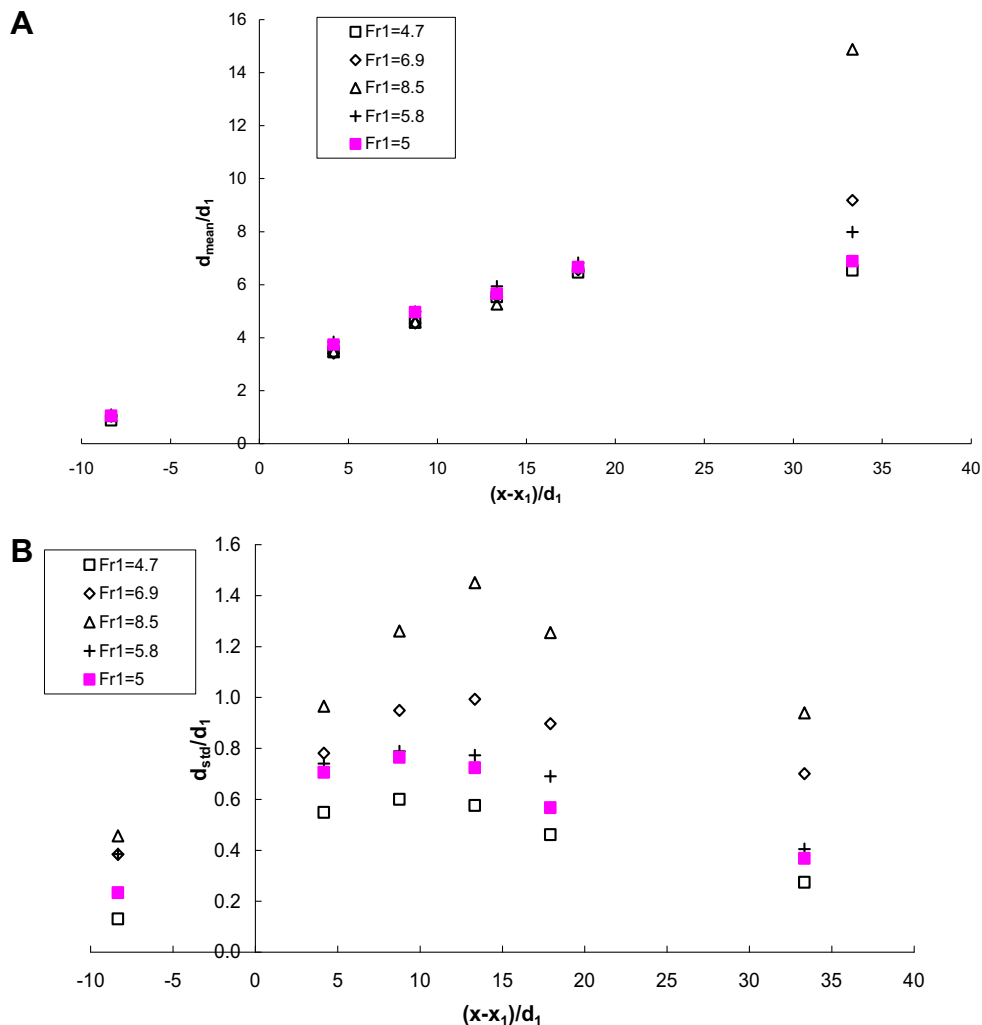
Fig. 3. Free surface profile along the hydraulic jump: (A) variation of mean flow depth and (B) variation of standard deviation of the flow depth.
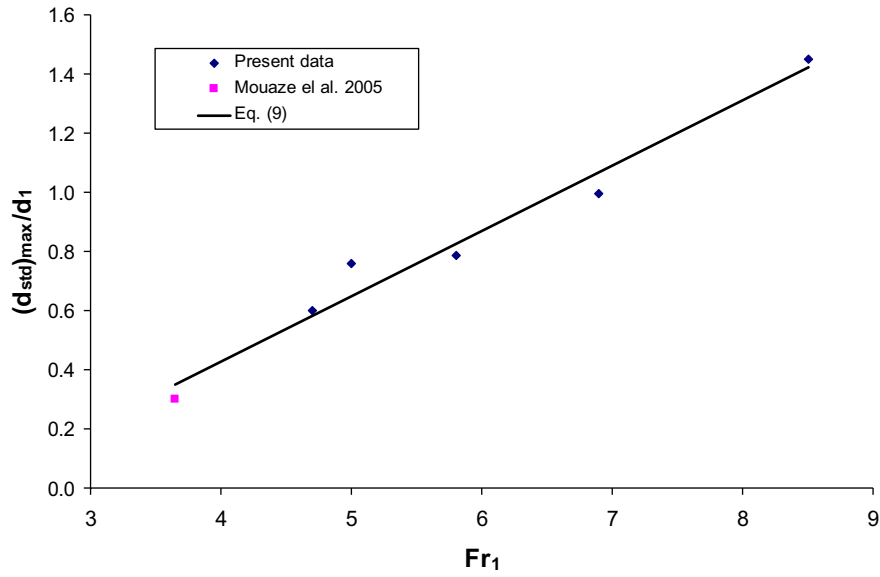
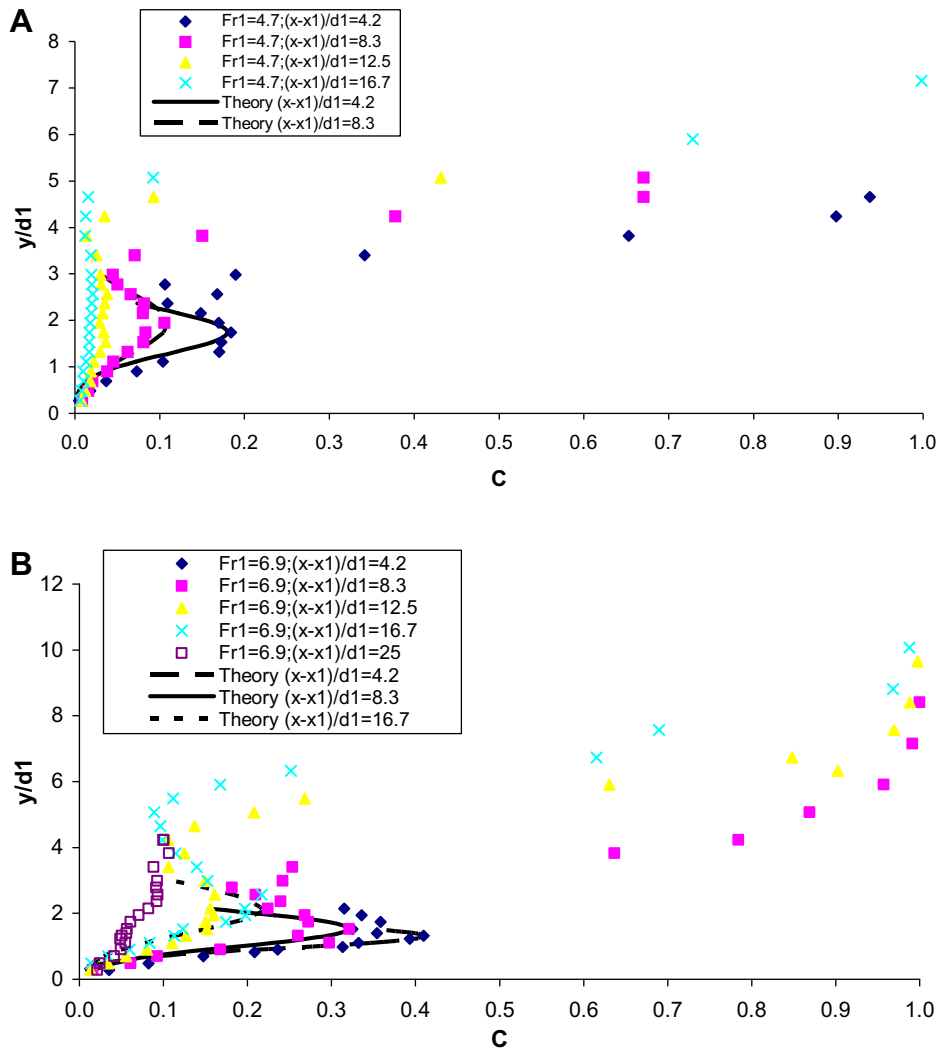**Fig. 4.** Variation of the maximum free-surface fluctuation with a function of Fr_1 number.

Fig. 5. Air concentration distribution along the hydraulic jump: (A) $Fr_1 = 4.7$ and (B) $Fr_1 = 6.9$.
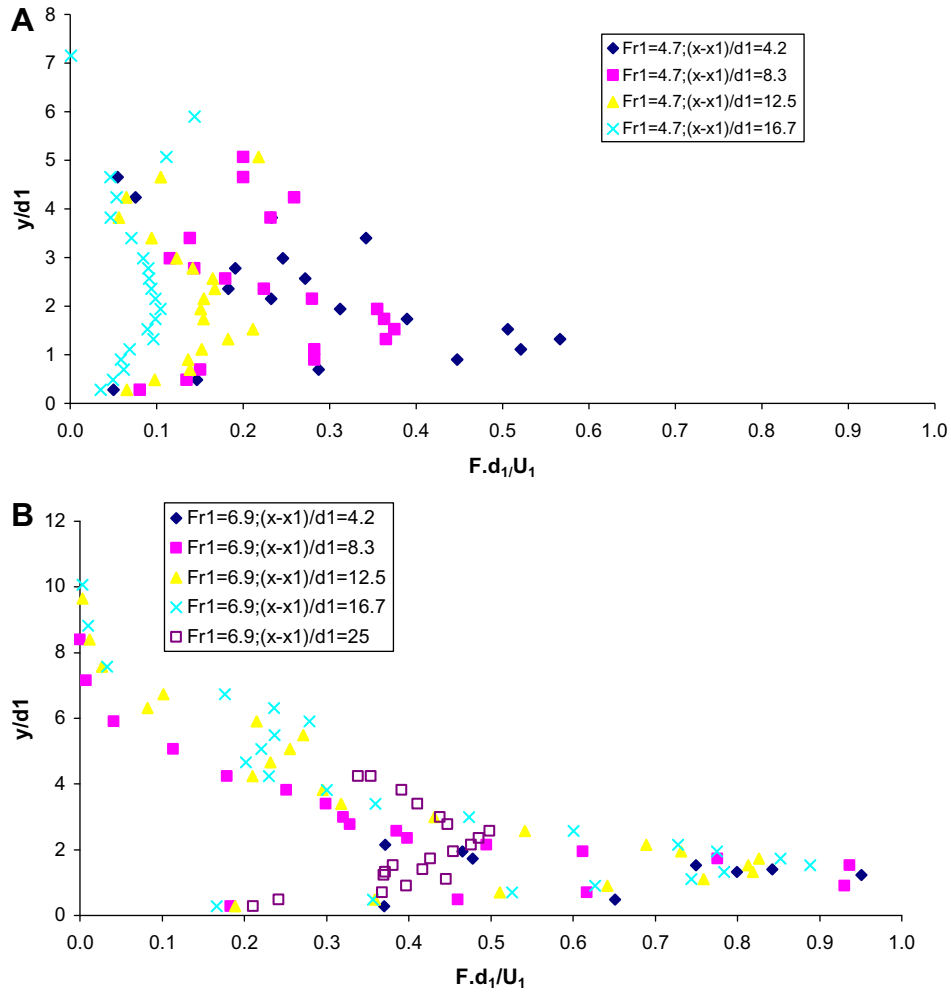
Fig. 6. Dimensionless bubble count rate distribution along the hydraulic jump: (A) $Fr_1 = 4.7$ and (B) $Fr_1 = 6.9$.
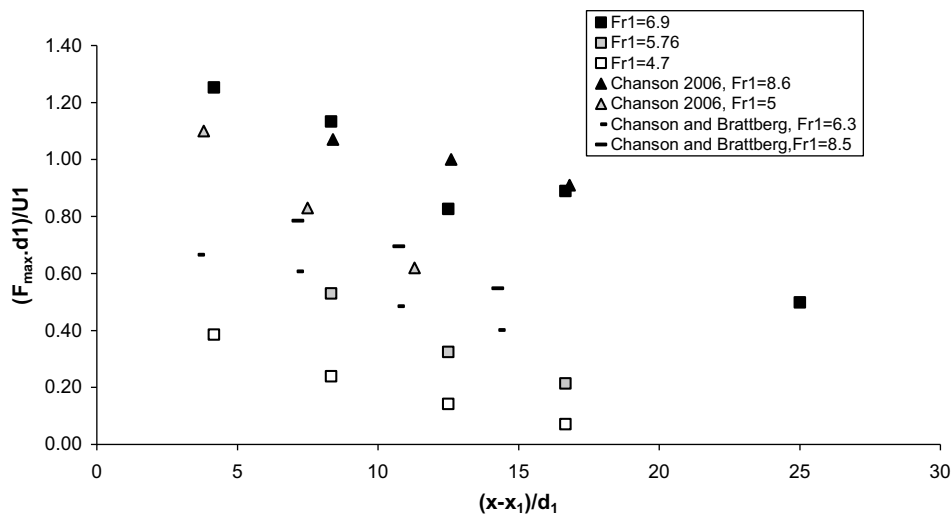

Fig. 7. Maximum dimensionless bubble count rate variation through the hydraulic jump for various Froude numbers.

shear layer which was characterized by intensive turbulence production, predominantly in vortices with horizontal axes perpendicular to the flow direction. The air packets were broken up in very small air bubbles as they were entrained in the shear region and the mixing layer was characterized by both large air content and maximum bubble count rates. Once the entrained bubbles were advected into regions of lesser shear, bubble coalescence led to the formation of larger air bubbles which were driven by buoyancy

towards the free-surface. In the recirculation region above the free shear layer, strong unsteady flow recirculation occurred.

3.1. Turbulent fluctuations of the free-surface

Typical mean surface profile (d_{mean}/d_1) and free-surface fluctuation (d_{std}/d_1) are presented in Fig. 3A and B, respectively, for various inflow Froude numbers. Herein d_{mean} is the time-averaged flow depth and d_{std} is the standard deviation of the flow depth. The data were deduced from the ultrasonic sensor signals.

The time-averaged water depth data showed a longitudinal surface profile that was consistent with visual observations and side photographs of the hydraulic jumps. For example, let us compare Figs. 1B and 3A. The standard deviations of the water depth data exhibited a rapid increase with increasing distance from the jump toe immediately downstream of the jump toe, highlighting the formation of the jump (Fig. 3B). These large fluctuations in free-surface elevations reflected the unsteady, dynamic nature of the hydraulic jump, caused possibly by the production, break up and pairing of macro-scale turbulent vortices in the developing shear layer. The water depth fluctuation upstream of the jump toe is not zero. The upstream flow is turbulent and some water depth fluctuations must be expected. Upstream of the jump, $(x - x_1)/d_1 < 0$, the free-surface profile was flat with small fluctuations

($d_{std}/d_1 > 0$). The reason of this could the horizontal oscillations of the jump toe. As the recent studies demonstrated [14], the jump toe oscillation frequencies took higher values with increasing upstream Froude number and this situation is consistent with the free-surface fluctuations. The maximum standard deviations of the water depth were typically seen for $10 \leqslant (x - x_1)/d_1 \leqslant 15$ (Fig. 3B). A linear relationship was observed herein between the maximum dimensionless free-surface fluctuation $(d_{std})_{max}/d_1$ and the inflow Froude number Fr_1. This is illustrated in Fig. 4 where the data are compared with a best fit relationship

$$\frac{(d_{std})_{max}}{d_1} = 0.23 \times Fr_1 - 0.52 \quad \text{for } 2.4 \leqslant Fr_1 \leqslant 8.5 \tag{9}$$

Eq. (9) is compared with the present experimental data and datum obtained by Mouaze et al. [13] in Fig. 4.

4. Distributions of void fraction and bubble count rate

Air bubble entrainment occurred in the form of air bubbles and air packets which were entrapped at the impingement of the upstream jet flow with the roller. Typical void fraction distributions in the hydraulic jump are shown in Fig. 5 for two inflow Froude numbers. Each graph presents the vertical distributions of void frac-
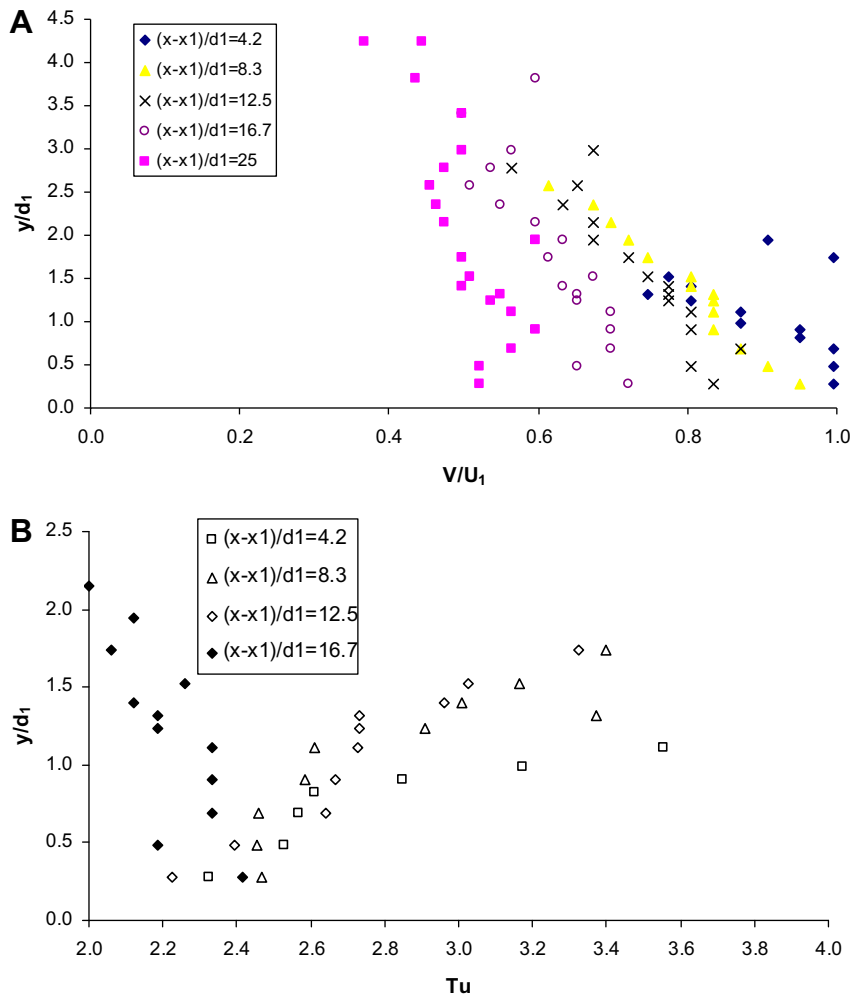

Fig. 8. Dimensionless distributions of turbulent velocity in hydraulic jumps with partially-developed inflow conditions: (A) dimensionless distributions of interfacial velocity V/U_1 in the hydraulic jump: $Fr_1 = 6.9$, $x_1 = 1$ m, $d_1 = 0.024$ m and (B) dimensionless distributions of streamwise turbulent intensity Tu in the hydraulic jump: $Fr_1 = 6.9$, $x_1 = 1$ m, $d_1 = 0.024$ m.

tion C as function of the dimensionless distance above the invert y/d_1 at several dimensionless distances from the jump toe $(x - x_1)/d_1$. The void fraction distribution data exhibited a marked maximum in the turbulent shear layer (Fig. 5). Such a result was previously observed in hydraulic jumps with partially-developed inflow conditions [5,23]. In the mixing layer, the distributions of void fraction followed a Gaussian distribution first proposed by Chanson [19,23]

$$C = C_{max} \times \exp\left(-\frac{\left(\frac{y - Y_{C_{max}}}{d_1}\right)^2}{4 \times D^{\#} \times \frac{x - x_1}{d_1}} \right) \qquad (10)$$

where $Y_{C_{max}}$ is the vertical elevation of the maximum void fraction C_{max}, $D^{\#} = D_t/(U_1 \times d_1)$ is a dimensionless air bubble diffusion coefficient, D_t is the turbulent diffusivity which averages the effects of turbulent diffusion and longitudinal velocity gradient, x and y are the longitudinal and vertical distances measured from the channel intake and bed, respectively, x_1 is the jump toe location, and d_1 is the inflow depth.

Eq. (10) is compared with some experimental data in Fig. 5. Eq. (10) is an approximate expression of the analytical solution of the advective diffusion equation for air bubbles [19]. It was found valid for hydraulic jumps with partially-developed inflow conditions and was validated with several data sets [5,7–9,23].

At the larger inflow Froude numbers, the present data showed that the advected air was more thoroughly dispersed, and it remained submerged for a longer distance from the jump toe (e.g. Fig. 5B). A comparison between Fig. 5A and B suggests that both the maximum void fractions and the length of the air–water shear layer increased with increasing inflow Froude numbers. The finding is in agreement with the work of Gualtieri and Chanson [24] in a smaller channel. The distributions of bubble count rate exhibited a characteristic shape with a distinct maximum F_{max} in the air–water shear layer. This is illustrated in Fig. 6 presenting some dimensionless distributions of bubble count rate at several longitudinal locations for two Froude numbers

($Fr_1 = 4.7$ and 6.9). The present data showed also a second, smaller peak in bubble count rate in the upper flow region for $C \sim 0.4$–0.5. The dominant bubble count rate peak F_{max} was located in the developing shear layer. This was first reported by Chanson and Brattberg [7] and further documented by Murzyn et al. [8] and Chanson [9]. It is believed to derive from the high levels of turbulent shear stresses in the air–water shear layer that break up the entrained air bubbles into finer air entities. The present experimental observations showed that the maximum count rate decreased with increasing distances from the jump toe. This is illustrated in Fig. 7, where the maximum dimensionless bubble count rate is plotted as a function of the longitudinal distance from the jump toe. The trend was consistent with some earlier observations [7–9].

5. Air–water turbulent velocity properties

Some velocity measurements were conducted in the hydraulic jump for one inflow Froude number ($Fr_1 = 6.9$), and some results are shown in Fig. 8. Fig. 8A presents some typical dimensionless velocity profiles in the shear region, while Fig. 8B shows some dimensionless distributions of turbulence intensity. Note that the velocity measurements were not conducted in the recirculation region nor near the free-surface, because the phase-detection intrusive probes could not discriminate the direction nor magnitude of the velocity in complicated turbulent flows. In the present study, the distributions of interfacial velocity showed a decreasing velocity with increasing distance from the invert, while the magnitude of the velocity decreased with increasing distance from the jump toe at a given elevation (Fig. 8A). The results were similar to velocity profiles in a wall jet. The analogy with the wall jet was first introduced by Rajaratnam [25] and later documented in the air–water flow region by Chanson and Brattberg [7]. It is illustrated in Fig. 9, where the interfacial velocity measurements are compared with the wall jet velocity distributions
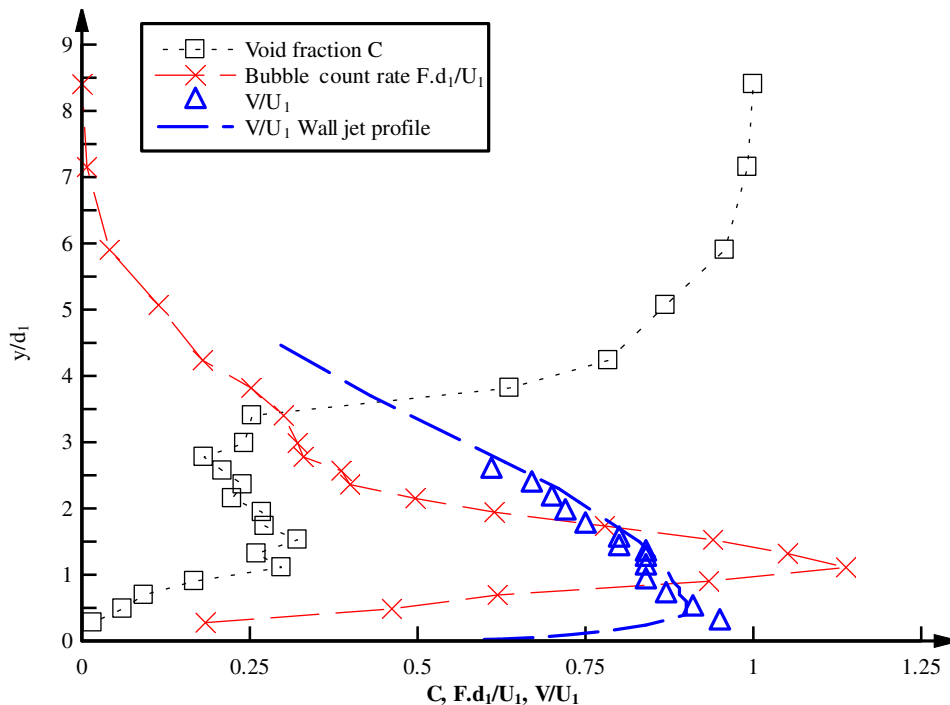

Fig. 9. Comparison between air and water velocity measurements in hydraulic jump and wall jet velocity distributions Eq. (11) – $Fr_1 = 6.9$, $x_1 = 1$ m, $d_1 = 0.024$ m, $x - x_1 = 0.2$ m.

$$\frac{V}{V_{\max}} = \left(\frac{y}{y_{V_{\max}}}\right)^{1/N} \quad \text{for } y/y_{V_{\max}} < 1 \tag{11A}$$

$$\frac{V}{V_{\max}} = \exp\left(-\frac{1}{2} \times \left(1.765 \times \left(\frac{y - y_{V_{\max}}}{y_{0.5}}\right)\right)^2\right) \quad \text{for } y/y_{V_{\max}} > 1 \tag{11B}$$

where $V_{\max}$ is the maximum velocity measured at $y = y_{V_{\max}}$, and $y_{0.5}$ is the distance (m) normal to invert where $V = V_{\max}/2$. Eq. (11) is compared with past and present experimental data in Fig. 9. Fig. 8B presents the distributions of turbulence levels Tu in the hydraulic jump. The turbulence intensities were large with typical values between 200% and 350% in the turbulent shear layer. For comparison, Resch and Leutheusser [5] obtained fluctuations of the water-phase velocities of about $Tu \sim 20$–100% using a hot-film probe with some crude signal processing. The difference of turbulence levels between the present study and Resch and Leutheusser [5] could be because of the different experimental techniques used in these studies. With a Prandtl–Pitot tube, Chanson and Brattberg [7] reported turbulence intensities between 20% and 40% in the clear-water region next to the invert ($y/d_1 < 1$). Interestingly, the present data indicated a marked redistribution of the turbulence intensity around $(x - x_1) = 0.4$ m with a relatively more uniform vertical distribution for $(x - x_1) \geqslant 0.4$ m (Fig. 8B). Rouse et al. [10] and Resch and Leutheusser [5] observed similarly some relatively uniform profiles of turbulent intensity in their experiments. It is suggested that buoyancy effects become preponderant for $(x - x_1)/d_1 \geqslant 16$, and bubble detrainment yielded lower void fractions and bubble count rates, hence lower interfacial velocity fluctuations.
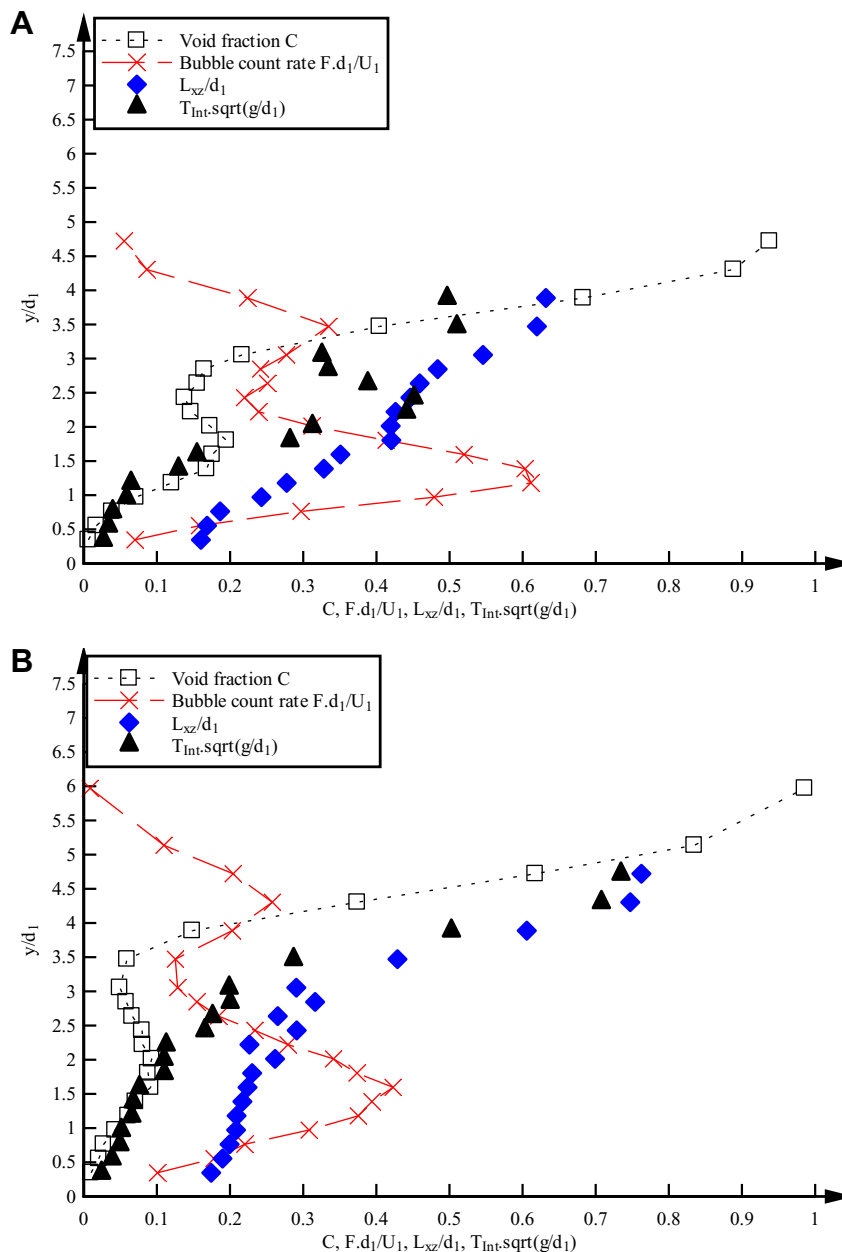

Fig. 10. Dimensionless distributions of integral turbulent time and length scales (L_{xz}/d_1 and $T_{Int} \times g/d_1$), void fraction and bubble count rate – $Fr_1 = 4.7$, $x_1 = 1$ m, $d_1 = 0.24$ m: (A) $(x - x_1)/d_1 = 4.2$, (B) $(x - x_1)/d_1 = 8.3$, (C) $(x - x_1)/d_1 = 12.4$, and (D) $(x - x_1)/d_1 = 16.7$.
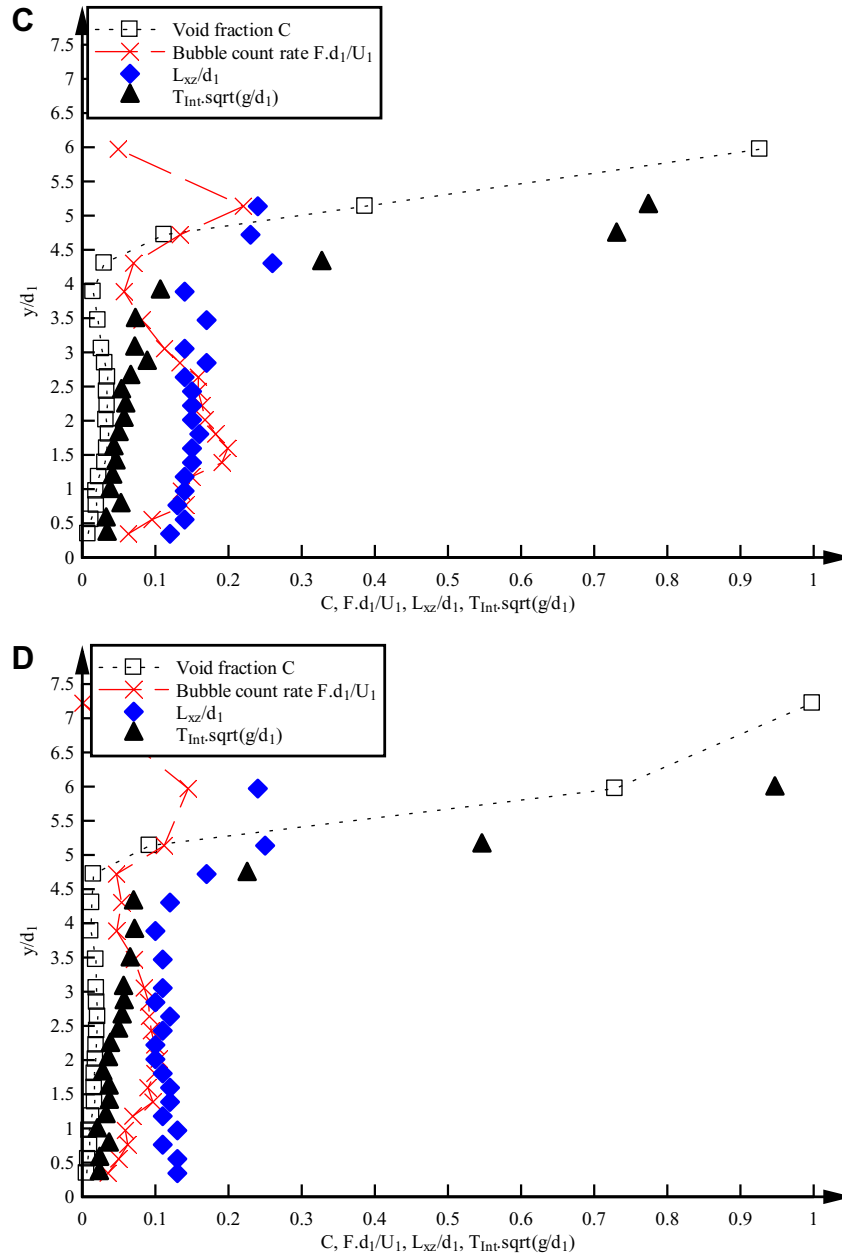
Fig. 10 (*continued*)

6. Turbulent integral time and length scales

The analysis of the phase-detection probe signal outputs provided some information on the turbulent time and length scales when some experiments were conducted with two identical probes separated by a known transverse distance z and simultaneously sampled at high-frequency (Fig. 3). Some correlation analyses were performed on the probe signal outputs using the method of Chanson [9] and Chanson and Carosi [21]. The basic correlation results included the air–water integral length and time scales, L_{xz} and T_{Int} which were calculated using Eqs. (6) and (7), respectively. They were deduced from identical experiments which were repeated for a range of probe separation distances z. The length scale L_{xz} is an integral air–water turbulence length scale which characterized the transverse size of the large vortical structures advecting the air bubbles in the hydraulic jump flows. It was a function of the inflow conditions, of the streamwise position

$(x - x_1)/d_1$ and vertical elevation y/d_1. Typical dimensionless distributions of integral length scales L_{xz}/d_1 are presented in Fig. 10. The void fraction and bubble count rate distributions are also shown for completeness. Fig. 10 illustrates some effect of the vertical elevation y/d_1 on the integral air–water turbulent length scale. Typically the integral length scale L_{xz} increased with increasing distance from the channel bed, and the dimensionless integral turbulent length scale L_{xz}/d_1 was typically between 0.2 and 0.8. The results were overall in close agreement with the experimental data of Chanson [9]. They suggested further some correlation between the void fraction and the integral length scale L_{xz}. For example, in Fig. 10A and C. The integral turbulent time scale results were consistent with the integral length scale data. Some comparative results are presented in Fig. 10. The data showed further a solid correlation between the integral time scale T_{Int} and the integral length scale L_{xz} for all inflow Froude numbers and longitudinal locations (Fig. 10).

7. Discussion

In hydraulic jumps with partially-developed inflow conditions, the void fraction and bubble count rate profiles showed consistently two distinct regions: (a) the turbulent shear region and (b) the upper region (e.g. Figs. 5 and 6). In the air–water shear region, the void fraction distributions exhibited a marked maximum C_{max}, which was always located above the location of the maximum bubble count rate F_{max}. The experimental observations showed systematically that the maximum void fraction C_{max} and maximum bubble count rate F_{max} were functions of the inflow Froude number Fr_1, of the inflow Reynolds number Re and of the streamwise position $(x - x_1)/d_1$. The present results highlighted the influence of the inflow Froude number on the air entrainment processes. At the highest Froude numbers, the entrained air bubbles were more thoroughly dispersed, and the largest amount of entrained air and bubble count rates were detected in the turbulent shear layer.

The present results showed furthermore negligible cross-correlations between two-phase-detection probes for transverse separation distance $z/d_1 > 0.6$–0.8. The finding implied that any transverse length scale of the bubbly shear flow must be smaller than about $0.8 \times d_1$. The integral turbulent length and time scale results were consistent with the earlier study of Chanson [9]. Interestingly the integral turbulent length and time scales may be compared with the experimental results of Chanson and Carosi [21]. Their experiments were conducted in a large stepped channel, and the same instrumentation and signal processing technique were applied. In skimming flows, air bubble entrainment takes place in the form of some interfacial aeration, and the entrained bubbles are advected in a boundary layer flow. In contrast, air entrainment in hydraulic jumps is a form of singular aeration: i.e. the air bubbles are entrapped at the jump toe (Fig. 1A). The entrained bubbles are advected in a developing shear layer, and there is some competition between the advective diffusion of air bubbles and of vorticity [19].

Some comparative results are presented in Fig. 11, where the dimensionless turbulence scales L_{xz}/d_c and $T_{Int} \times g/d_c$ are presented as functions of the void fraction, with d_c the critical flow depth ($d_c = \sqrt[3]{q^2/g}$), and q is the water discharge per unit width. The results illustrated some differences between hydraulic jump and
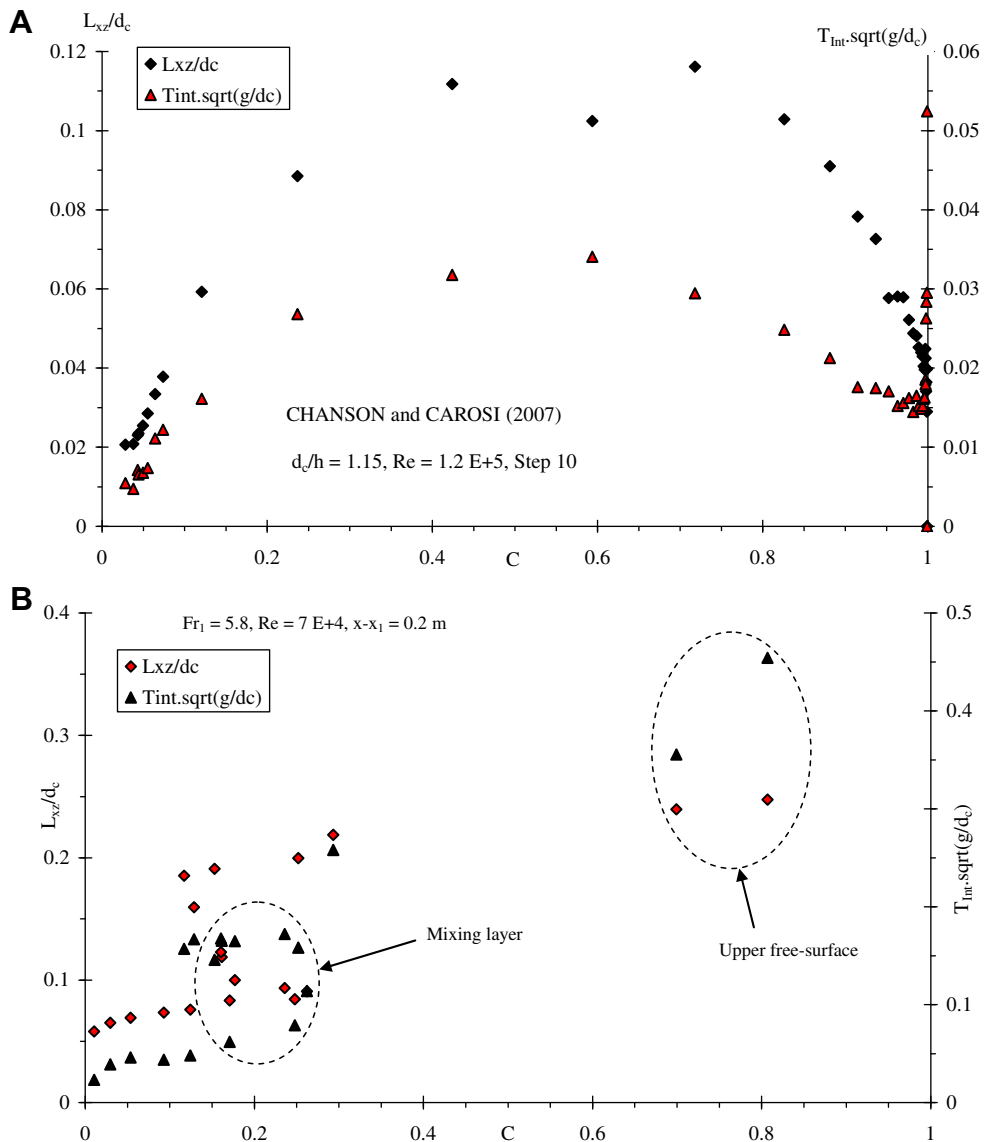

Fig. 11. Dimensionless relationship between void fraction and integral turbulent time and length scales (L_{xz}/d_c, $T_{Int} \times g/d_c$): (A) skimming flow data [21] – $d_c/h = 1.15$, $h = 0.10$ m, $Re = 1.2 \times 10^5$, $d_c = 0.115$ m, Step 10 and (B) hydraulic jump flow (present study) – $Fr_1 = 5.8$, $Re = 7 \times 10^4$, $x_1 = 1$ m, $d_c = 0.077$ m.

skimming flow in terms of integral turbulent scales (Fig. 11). The quantitative results in skimming flow and in the shear layer of the hydraulic jump were comparable. But substantial differences were observed in the upper flow region of the hydraulic jump flow (Fig. 11B).

These differences may reflect the recirculation nature of roller upper surface, whereas the skimming flow free-surface region is the locus of interfacial aeration with lesser vorticity levels.

8. Conclusion

New air–water flow measurements were performed in hydraulic jumps with partially-developed inflow conditions for a range of inflow Froude numbers $4.7 \leqslant Fr_1 \leqslant 8.5$. The experiments were conducted in a large-size facility using two types of phase-detection intrusive probes, complemented by some measurements of the free-surface fluctuations using ultrasonic displacement meters. The new study was focused on the air–water turbulence characteristics in the turbulent shear layer of hydraulic jumps with partially-developed inflow conditions. The free-surface fluctuation measurements showed large turbulent fluctuations that reflected the dynamic unsteady structure of the hydraulic jump flows. A linear relationship was found between the normalized maximum free-surface fluctuation and the inflow Froude number. The void fraction measurements showed the presence of an advective diffusion shear layer in which the void fractions profiles followed closely an analytical solution of the advective diffusion equation for air bubbles. A similar finding was observed in earlier studies of hydraulic jumps with partially-developed inflow conditions. In the air–water shear layer, the distributions of void fraction and bubble count rate exhibited both a marked maximum. The velocity profiles tended to follow a wall jet flow pattern, with a decreasing interfacial velocity with increasing distance from the jump toe.

The air–water turbulent integral time and length scales were deduced from auto- and cross-correlation analyses based upon the method of Chanson [9]. The result provided some characteristic transverse time and length scales of the eddy structures advecting the air bubbles in the developing shear layer. The dimensionless turbulent integral length scales L_{xz}/d_1 were closely related to the inflow depth: i.e. $L_{xz}/d_1 = 0.2$–0.8, with L_{xz} increasing towards the free-surface.

The writers believe that the present results bring some new light to a better understanding of turbulent processes in hydraulic jump flows and of the interactions between entrained air and turbulent structures. The results could have important implications in terms of civil and environmental engineering structures.

Acknowledgments

References

[1] J.B. Belanger, Essai sur la Solution Numérique de quelques Problèmes Relatifs au Mouvement Permanent des Eaux Courantes (Essay on the Numerical Solution of Some Problems relative to Steady Flow of Water), Carilian-Goeury, Paris, 1828 (in French).
[2] F.M. Henderson, Open Channel Flow, MacMillan Company, New York, 1966.
[3] H. Chanson, The Hydraulics of Open Channel Flow: An Introduction, Butterworth-Heinemann, Oxford, 2004.
[4] N. Rajaratnam, An experimental study of air entrainment characteristics of the hydraulic jump, J. Inst. Eng. India 42 (7) (1962) 247–273.
[5] F.J. Resch, H.J. Leutheusser, Le Ressaut Hydraulique: Mesure de turbulence dans la région diphasique (the hydraulic jump: turbulence measurements in the two-phase flow region), J La Houille Blanche 4 (1972) 279–293 (in French).
[6] M. Mossa, U. Tolve, Flow visualization in bubbly two-phase hydraulic jump, J. Fluids Eng., ASME 120 (1998) 160–165.
[7] H. Chanson, T. Brattberg, Experimental study of the air–water shear flow in a hydraulic jump, Int. J. Multiphase Flow 26 (4) (2000) 583–607.
[8] F. Murzyn, D. Mouaze, J.R. Chaplin, Optical fibre probe measurements of bubbly flow in hydraulic jumps, Int. J. Multiphase Flow 31 (1) (2005) 141–154.
[9] H. Chanson, Bubbly flow structure in hydraulic jump, Eur. J. Mech. B/Fluids 26 (3) (2007) 367–384.
[10] H. Rouse, T.T. Siao, S. Nagaratnam, Turbulence characteristics of the hydraulic jump, Trans. ASCE 124 (1959) 926–966.
[11] M. Liu, N. Rajaratnam, D. Z Zhu, Turbulent structure of hydraulic jumps of low Froude numbers, J. Hydraul. Eng., ASCE 130 (6) (2004) 511–520.
[12] H. Chanson, Air Bubble Entrainment in Hydraulic Jumps. Similitude and Scale Effects, Report No. CH57/05, Department of Civil Engineering, The University of Queensland, Brisbane, 2006.
[13] D. Mouaze, F. Murzyn, J.R. Chaplin, Free surface length scale estimation in hydraulic jumps, J. Fluids Eng., Trans. ASME 127 (2005) 1191–1193.
[14] F. Murzyn, H. Chanson, Free Surface, Bubbly flow and Turbulence Measurements in Hydraulic Jumps, Report CH63/07, Division of Civil Engineering, The University of Queensland, Brisbane, 2007.
[15] C. Crowe, M. Sommerfield, Y. Tsuji, Multiphase Flows with Droplets and Particles, CRC Press, Boca Raton, 1998.
[16] H. Chanson, Air–water flow measurements with intrusive phase-detection probes. Can we improve their interpretation?, J. Hydraul. Eng., ASCE 128 (3) (2002) 252–255.
[17] C. Koch, H. Chanson, Unsteady turbulence characteristics in an undular bore, in: Proceedings of the International Conference on Fluvial Hydraulics River Flow, Lisbon, 2006.
[18] H. Chanson, S. Aoki, M. Maruyama, Unsteady air bubble entrainment and detrainment at a plunging breaker: dominant time scales and similarity of water level variations, Coast. Eng. 46 (2) (2002) 139–157.
[19] H. Chanson, Air Bubble Entrainment in Free-Surface Turbulent Shear Flows, Academic Press, London, 1997.
[20] H. Chanson, L. Toombes, Air–water flows down stepped chutes: turbulence and flow structure observations, Int. J. Multiphase Flow 28 (11) (2002) 1737–1761.
[21] H. Chanson, G. Carosi, Turbulent time and length scale measurements in high-velocity open channel flows, Exp. Fluids 42 (3) (2007) 385–401.
[22] S. Kucukali, H. Chanson, Turbulence in Hydraulic Jumps: Experimental Measurements, Report No. CH62/07, Division of Civil Engineering, The University of Queensland, Brisbane, 2007.
[23] H. Chanson, Air entrainment in two-dimensional turbulent shear flows with partially developed inflow conditions, Int. J. Multiphase Flow 21 (6) (1995) 1107–1121.
[24] C. Gualtieri, H. Chanson, Experimental analysis of Froude number effect on air entrainment in the hydraulic jump, Env. Fluid Mech. 7 (3) (2007) 217–238.
[25] N. Rajaratnam, The hydraulic jump as a wall jet, J. Hydraul. Div., ASCE 91 (5) (1965) 107–132.